

Quantum Melting of Spin-1 Dimer Solid Induced by Inter-chain Couplings

Yi Xu,^{1,*} Tianfu Fu,¹ Juraj Hasik,^{2,3,†} and Andriy H. Nevidomskyy^{1,‡}

¹*Department of Physics and Astronomy, Rice University, Houston, TX 77005, USA*

²*Laboratoire de Physique Théorique UMR5152, C.N.R.S. and Université de Toulouse, 118 rte de Narbonne, 31062 Toulouse, FRANCE*

³*Institute for Theoretical Physics and Delta Institute for Theoretical Physics, University of Amsterdam, Science Park 904, 1098 XH Amsterdam, The Netherlands*

(Dated: September 22, 2022)

Dimerized valence bond solids appear naturally in spin-1/2 systems on bipartite lattices, with the geometric frustrations playing a key role both in their stability and the eventual ‘melting’ due to quantum fluctuations. Here, we ask the question of the stability of such dimerized solids in spin-1 systems, taking the anisotropic square lattice with bilinear and biquadratic spin-spin interactions as a paradigmatic model. The lattice can be viewed as a set of coupled spin-1 chains, which in the limit of vanishing inter-chain coupling are known to possess a stable dimer phase. We study this model using the density matrix renormalization group (DMRG) and infinite projected entangled-pair states (iPEPS) techniques, supplemented by the analytical mean-field and linear flavor wave theory calculations. While the latter predicts the dimer phase to remain stable up to a reasonably large interchain-to-intrachain coupling ratio $r \lesssim 0.6$, the DMRG and iPEPS find that the dimer solid melts for much weaker interchain coupling not exceeding $r \lesssim 0.15$. We find the transition into a magnetically ordered state to be first order, manifested by a hysteresis and order parameter jump, precluding the deconfined quantum critical scenario. The apparent lack of stability of dimerized phases in 2D spin-1 systems is indicative of strong quantum fluctuations that melt the dimer solid.

Dimerized valence bond solid (DVBS) is a magnetic analog of an atomic crystal, with the spin singlets on the non-overlapping links of a lattice forming a long-range order that spontaneously breaks the translation symmetry. Such DVBS are known to be the exact ground states of certain models [1, 2] and are expected to appear naturally in spin-1/2 systems on bipartite lattices, where extensive numerical studies using density matrix renormalization group (DMRG), variational Monte Carlo (VMC) and tensor-network methods corroborate that VBS phases (including plaquette VBS) are stable on the square [3–7] and honeycomb [8, 9] lattices. Of particular interest is the effect of geometric frustrations that enhance the quantum fluctuations which can “melt” the DVBS solid in favor of the resonating valence bond (RVB) state [10, 11] – a long sought-after quantum spin liquid in the paradigmatic $J_1 - J_2$ model on the square lattice [3–7]

While spin-1/2 models have been studied extensively, the appeal of higher-spin systems (where S is not too large so as not to become quasi-classical) is that they allow for non-geometric frustration due to the nontrivial biquadratic interactions $(\mathbf{S}_i \cdot \mathbf{S}_j)^2$. The competition with the familiar Heisenberg term then results in a rich phase diagram that, in the case of two-dimensional (2D) $S = 1$ model can potentially host more exotic phases, including the ferroquadrupolar and antiferroquadrupolar (spin nematic) orders [12–18], as well as a putative quantum spin liquid that breaks the lattice point-group symmetry [19, 20]. Experimentally, compounds like NiGaS₂ [21–23] and Ba₃NiSb₂O₉ [24, 25] with $S = 1$ moments have been proposed to be close to the spin-nematic phases. Spin-1 model can also be fine-tuned to the SU(3)-symmetric points (there are two [26, 27])

which lend themselves to possible realization in ultracold alkaline-earth atoms [28].

This raises a question – to what extent the DVBS phases, so central to the discussion of the dimer models [29, 30] and RVB spin liquids [10, 11], are prevalent in higher spin models, in particular in spin-1 counterparts? In principle, spin singlet state is allowed to form on a pair of sites for an arbitrary spin representation of SU(2), so there is no fundamental obstruction. Yet numerical studies point to the lack of stability of DVBS states in SO(3)-symmetric spin-1 models on either the square or the honeycomb lattices in 2D [15, 31–33]. This is to be contrasted with 1D spin chains, where the DVBS state (sometimes called spin-Peierls state) is well documented in the bilinear-biquadratic spin-1 model [34, 35]. To understand the reason for this dichotomy, we consider the paradigmatic bilinear-biquadratic spin-1 model on an anisotropic square lattice with the vertical links weaker than the horizontal ones:

$$H = \sum_{i,j} \left[J_{\parallel} \mathbf{S}_{i,j} \cdot \mathbf{S}_{i+1,j} + K_{\parallel} (\mathbf{S}_{i,j} \cdot \mathbf{S}_{i+1,j})^2 \right] + \sum_{i,j} \left[J_{\perp} \mathbf{S}_{i,j} \cdot \mathbf{S}_{i,j+1} + K_{\perp} (\mathbf{S}_{i,j} \cdot \mathbf{S}_{i,j+1})^2 \right]. \quad (1)$$

The degree of the lattice anisotropy can be captured by the ratio $r \equiv J_{\perp}/J_{\parallel} = K_{\perp}/K_{\parallel}$ (we assume the last equality for simplicity, but it does not affect our conclusions qualitatively). Clearly, $r = 0$ corresponds to the limit of decoupled spin chains, for which we know the DVBS phase to be stable as long as K_{\parallel} is negative and $|K_{\parallel}| > |J_{\parallel}|$ [34, 35]. How far does this DVBS phase extend toward the isotropic square lattice limit ($r = 1$)?

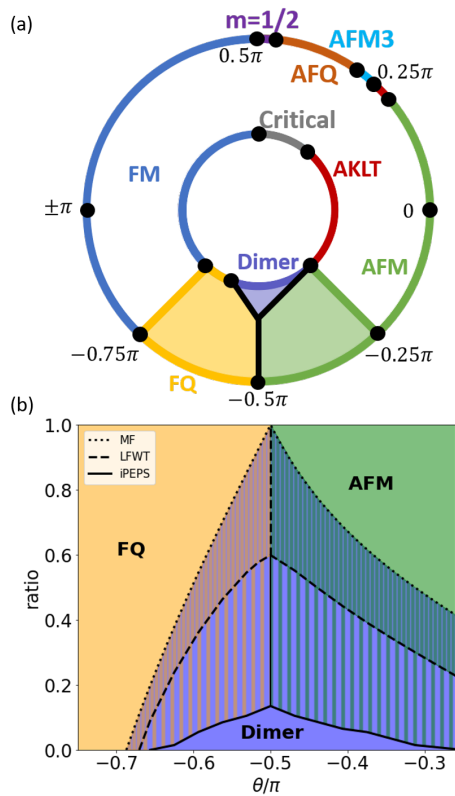


FIG. 1. (a) A schematic illustration of the piled-up phase diagrams for the spin-1 BBH chain (inner circle) and the spin-1 BBH model on the square lattice (outer circle), with the shaded region in-between representing the phase diagram of the coupled spin-1 BBH chains. The radial axis describes the relative strength of inter-chain couplings. (b) Phase diagram for the coupled spin-1 BBH chains, where mean-field, the linear flavor wave theory and iPEPS results are plotted. The solid lines indicate the actual phase boundaries, which are of first order.

To answer this question, in this Letter we have performed numerical analysis by two different tensor network methods, DMRG and infinite projected entangled-pair state (iPEPS), supplemented by the analytical mean-field (MF) and linear flavor-wave theory (LFWT) calculations. Our main findings are summarized in Fig. 1, utilizing the commonly used parametrization $J_{\parallel} = \cos \theta$, $K_{\parallel} = \sin \theta$ in terms of the polar angle θ . We find that a relatively weak interchain coupling ($r_c \lesssim 0.15$) is sufficient to melt the VBS solid, yielding one of the rotational-symmetry-broken long range ordered phases: either the Néel (at $\theta > -\pi/2$) or the ferroquadrupolar phase (at $-2\pi/3 \lesssim \theta < -\pi/2$). Since these phases break a different symmetry than the $SO(3)$ -symmetric VBS state, a direct second-order phase transition between such states is seemingly not allowed in the Landau-Ginzburg paradigm. However, when topological defects of either order parameter are considered, a field theory supporting a putative continuous phase transition between the VBS and Néel state can be written down, outlining the framework of so-called deconfined quantum

criticality [36, 37]. This provides a second motivation for the present study, namely: can the model in Eq. (1) support such a continuous phase transition? Our results show that the answer is negative, with a clear hysteresis indicating a first-order phase transition from the VBS into either the Néel or FQ ordered state.

DVBS phase. In 1D, the existence of the dimerized VBS phase is well established, with the simplest wavefunction being a product of dimers on alternating bonds along the decoupled chains:

$$|DVBS\rangle = \prod_j \prod_{i=2m+1} |\text{dimer}(S_{i,j}, S_{i+1,j})\rangle, \quad (2)$$

bearing in mind that the singlet state of two spins-1 is written as $|\text{dimer}(S_1, S_2)\rangle = \frac{1}{\sqrt{3}}(|1\bar{1}\rangle + |\bar{1}1\rangle - |00\rangle)$. The corresponding dimer order parameter D_h is defined by

$$\langle D_h \rangle = \langle \mathbf{S}_{i,j} \cdot \mathbf{S}_{i+1,j} \rangle - \langle \mathbf{S}_{i+1,j} \cdot \mathbf{S}_{i+2,j} \rangle. \quad (3)$$

Note that the $|DVBS\rangle$ ansatz is a zero-length entangled state with no correlation between the dimers, achieving the maximal possible $|\langle D_h \rangle| = S(S+1) = 2$. A most general dimer state need not be a product state, and correlations can develop between the dimers; in all cases a non-vanishing Landau order parameter (3) serves as a definition of the DVBS long-range order [38].

Competing phases. In the 2D limit of isotropic square lattice ($r = 1$), prior iPEPS results find no DVBS phase [15], instead the interval $\theta \in [-3\pi/4, -\pi/4]$ is occupied by the FQ (yellow) and Néel (green) phases, as indicated in Fig. 1a. The Néel phase is characterized by the staggered magnetization m_s . The FQ phase, on the other hand, features a vanishing magnetic moment $\langle \mathbf{S} \rangle = \mathbf{0}$, but breaks the $SO(3)$ spin symmetry in a more subtle way. Namely, FQ phase can be written (up to an overall phase) as a linear superposition with *real* coefficients of three quadrupolar basis states $|x\rangle = \frac{i}{\sqrt{2}}(|1\rangle - |\bar{1}\rangle)$, $|y\rangle = \frac{1}{\sqrt{2}}(|1\rangle + |\bar{1}\rangle)$, $|z\rangle = -i|0\rangle$ [39]:

$$|FQ\rangle = d_x|x\rangle + d_y|y\rangle + d_z|z\rangle. \quad (4)$$

The real coefficients d_α form the components of a director, which spontaneously breaks the $SO(3)$ symmetry. One can show that the FQ state has a non-zero value of the ferroquadrupolar operators defined as a traceless symmetric tensor $\hat{Q}^{\alpha\beta} \equiv \hat{S}^\alpha \hat{S}^\beta + \hat{S}^\beta \hat{S}^\alpha - \frac{2}{3}S(S+1)\delta_{\alpha\beta}$. One way to define the FQ order parameter is proportional to the trace of this matrix squared: $II_Q = -\frac{1}{2}\text{Tr}(\langle \hat{Q} \rangle^2)$ [15].

Mean-field and LFWT insights. Using the product state ansätze for the Néel, FQ and DVBS phases, we obtain the expressions for the mean-field energies (see SM):

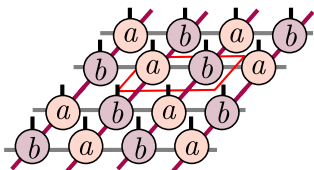
$$\begin{aligned} E_N^{\text{mf}}(r) &= -(1+r)\cos\theta + (S^2+1)(1+r)\sin\theta \\ E_{\text{FQ}}^{\text{mf}}(r) &= (S^2 + \frac{1}{2} + \frac{1}{2}\Theta(\frac{5}{4} - S))(1+r)\sin\theta \\ E_{\text{DVBS}}^{\text{mf}}(r) &= -\frac{S+1}{2S}\cos\theta + \frac{(S+1)^2}{3}(2+r)\sin\theta, \end{aligned} \quad (5)$$

which for $S = 1$ results in the transitions indicated by the dotted lines in Fig. 1b. The mean-field treatment overestimates the stability of the DVBS phase and we use the linear flavour-wave theory to account for the quantum fluctuations around the FQ and Néel phase, respectively. Starting from the Néel phase, the LFWT treatment is equivalent to the Holstein–Primakoff bosons, with the resulting energy lowered by the zero-point fluctuations (see SM). The flavor-wave expansion around the FQ order requires more care, representing the spin operators S^α and quadrupolar operators $Q^{\alpha\beta}$ in terms of the bilinears of the three flavors of Schwinger bosons forming a fundamental representation of group $SU(3)$, namely: $S^\alpha = -i\varepsilon_{\alpha\beta\gamma}b_\beta^\dagger b_\gamma$, $Q^{\alpha\beta} = \frac{2}{3}\delta_{\alpha\beta} - b_\alpha^\dagger b_\beta - b_\beta^\dagger b_\alpha$. One then treats the FQ phase as a Bose–Einstein condensation of one of the boson flavors $\langle b_z \rangle \neq 0$, and uses the constraint $\sum_\alpha b_\alpha^\dagger b_\alpha = 1$ to express the condensate fraction as

$$\langle b_z \rangle = \sqrt{1 - b_x^\dagger b_x - b_y^\dagger b_y}, \quad (6)$$

where expanding the square root to first order in boson bilinears amounts to LFWT. Diagonalizing the resulting Hamiltonian and computing the zero-point energy correction to the mean-field expression (5) makes the FQ and Néel phases more energetically favourable, thus lowering the critical value r_c at which the VBS phase melts, shown by the dashed line in Fig. 1b.

iPEPS. In order to provide an unbiased corroboration of the above LFWT results, we have used the iPEPS method [40], which has been previously demonstrated to describe well both the FQ and Néel order of spin-1 on the square lattice [15]. In iPEPS, the wavefunction on the (infinite) square lattice is written in terms of a product of tensors, with the contraction over the auxiliary indices that are defined on the links of the lattice. Based on the known phases in 1D and 2D, we choose the bipartite tiling by a 2×1 unit cell containing two distinct tensors a and b which we then variationally optimize [41]. Such ansatz can describe the staggered pattern of the Néel ordered states as well as the DVBS covering



$$|\psi(a, b)\rangle = \dots \quad (7)$$

The physical indices associated to physical spin $S = 1$ degrees of freedom are represented by black vertical lines. The approximation is controlled by the bond dimensions of auxiliary indices in horizontal (gray indices l, r) and vertical direction (magenta u, d), now denoted D_x and D_y respectively, which need not to be the same. Indeed, the decoupled chain limit $r \rightarrow 0$ can be described just with $D_y = 1$. Evaluation of energy and order parameters requires additional *environment* tensors whose precision

is controlled by their environment dimension χ , here constructed by corner transfer matrix method [42]. In our simulations, we found it sufficient to set $D_x = 9$, $D_y = 4$ and $\chi = 16$ in order to obtain well converged results in all three phases ($D_x = 9$ turns out to be the minimal bond dimension that allows to realize a variationally competitive $SU(2)$ -symmetric DVBS state in the limit of decoupled chains). To verify, we have run the iPEPS calculations with more exacting parameters ($D_x = 9$, $D_y = 6$, and χ up to 32) at several points in each phase, which gave nearly identical results. The relatively small environment dimension χ necessary to obtain converged results points to the short correlation lengths of optimized iPEPS in the competing ordered phases. We refer the reader to the Supplementary Materials for further details of the iPEPS simulations.

The resulting phase diagram is shown in Fig. 1b and Fig. 2e, with the solid black line indicating the boundary of the DVBS phase. It is immediately apparent that a small value of interchain coupling (anisotropy ratio $r_c \lesssim 0.15$) is sufficient to melt the DVBS phase in favor of a long-range ordered magnetic or nematic (Néel or FQ) phase. This is completely consistent with the prior iPEPS results on the isotropic square lattice ($r = 1$) where the DVBS order is conspicuously absent [15].

DMRG. As a complementary method, we also use the density matrix renormalization group method to simulate the coupled chains. DMRG is a numerical method first proposed to study 1D systems [43] and subsequently generalized to the studies of finite 2D systems in a cylindrical geometry [44]. Aligning the chains along the cylinder direction (x) with open boundary conditions, we chose long cylinders of dimension $N_x \times N_y$ with $N_x = 30 - 80$ to minimize the effect of the boundaries. The results were then extrapolated to the 1D thermodynamic limit $N_x \rightarrow \infty$. The computational complexity grows exponentially with the cylinder circumference, which was therefore kept at $N_y = 4$ for most of the calculations. We checked that larger $N_y = 6$ simulations do not qualitatively change our conclusion. We used DMRG implementation provided by ITensor library [45], with explicit $U(1)$ symmetry. The maximum number of states kept in our simulations were $M = 1600$, achieving acceptable truncation errors less than 8×10^{-5} .

It turns out that cylinders of $N_y = 4$ are able to capture the phase transitions as the DVBS order melts very quickly even with weak inter-chain couplings, corroborating our iPEPS results. Shown in Fig. 3 are the two orders parameters along the DVBS–Néel phase transition, averaged over the middle portion $\Delta N_x \times N_y = 12 \times 4$ of the cylinders for all N_x so as to avoid the boundary effects. We note in passing that care must be taken in computing the order parameter in DMRG, since spontaneous breaking of the $SO(3)$ spin symmetry is only possible in the thermodynamic limit. To overcome this, we introduced

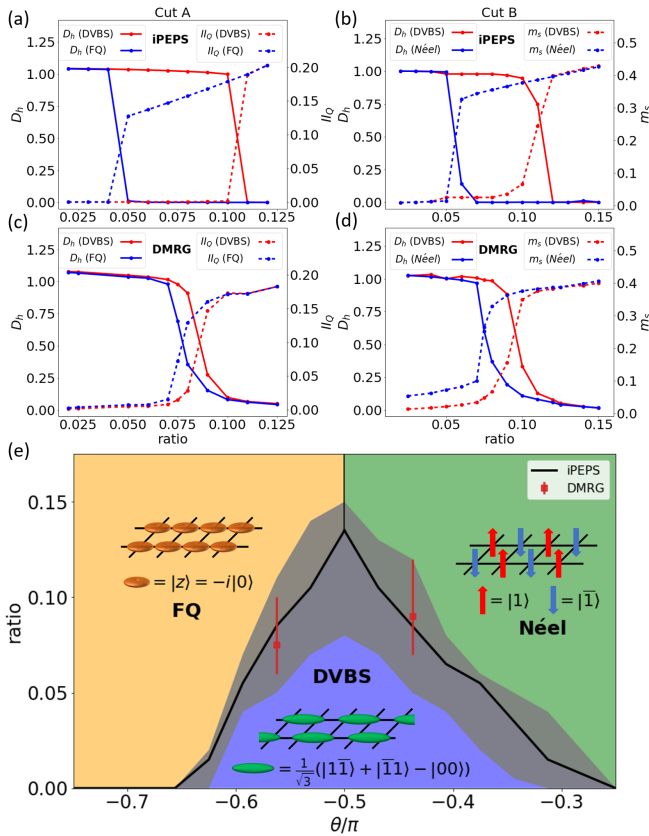


FIG. 2. Hysteresis. (a)-(d) Order parameters for cut A ($\theta = -0.5625\pi$) and B ($\theta = -0.4375\pi$). States for each ratio are optimized using both dimerized initial states (blue curves) and ferroquadrupolar states (red curves). (e) Hysteresis is indicated by shaded region (iPEPS) and errorbars (DMRG).

the pinning fields on the open boundaries of the cylinder (see SM for more details), as is the standard practice in $U(1)$ -symmetric DMRG calculations.

It is clear from the order parameter plots Fig. 3 that there is a (narrow) regime of coexistence, indicating that the DVBS–Néel transition is first order. To further corroborate this finding, we analyze below the hysteresis of both this and the DVBS–FQ transition.

Hysteretic melting of the DVBS order. We corroborate the first-order nature of the phase transitions from DVBS phase by observing the hysteresis. Indeed, we found that the critical value r_c at which the DVBS phase melts depends on the choice of the initialization in DMRG (or the initial choice of tensors in iPEPS). To systematically investigate this effect, we have prepared the initial state to either be the $|\text{DVBS}\rangle$ product state in Eq. (2) or one of the ordered states: FQ for $\theta < -\pi/2$ (“cut A” in Fig. 2) or Néel for $\theta > -\pi/2$ (“cut B” in Fig. 2). We then plot the dimer order parameter $\langle D_h \rangle$ (solid lines in Fig. 2), which shows a clear hysteresis loop traced between the blue and red lines in Figs. 2a-2d depending on the choice of the initial condition. We similarly plot with the dashed

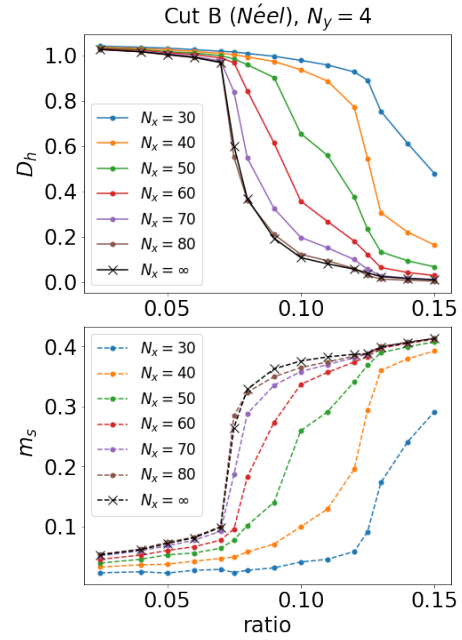


FIG. 3. Finite size scaling of the VBS order parameter D_h and the staggered magnetization m_s in DMRG calculations, plotted along the vertical cut B ($\theta = -0.4375\pi$) in the phase diagram (Fig. 2e). Different symbols/colors label the cylinder lengths N_x , extrapolated to the thermodynamic limit. The Néel AFM state was used to initialize the density matrices.

lines the FQ order parameter (II_Q , defined below Eq. 4) along cut A in Figs. 2(a,c) and the staggered magnetization m_s along cut B in Figs. 2(b,d). In all cases, a clear hysteresis associated with a discontinuous phase transition is observed. The width of the hysteresis is narrower in our DMRG data compared with iPEPS, which we attribute to the practical limitations on the circumference of the cylinder used in DMRG calculations.

We determine the position of the DVBS melting phase transition by following the energy level crossing between the two differently initialized configurations (see SM). The transition r_c thus obtained falls roughly halfway inside the hysteresis loop (greyed area in the phase diagram Fig. 2e) – this is how the phase boundaries (solid black lines) were obtained in Figs. 1b and 2e. We have also verified that the correlation functions all remain short-ranged across the DVBS melting transition (see SM), again corroborating the discontinuous nature of the transition.

Discussion. As the comparison between the MF results, LFWT and DMRG/iPEPS indicates, quantum fluctuations tend to destabilize the dimerized VBS order even at very weak interchain couplings $r_c \lesssim 0.15$. We find that the DVBS state, even when stable, is not a simple product state such as in the MF ansatz (2), but that dimer-dimer correlations are pronounced, eventually melting the dimer order.

While the present study focuses on the frustration induced by the biquadratic interaction, the implications

hold for more general models with geometric frustrations. For instance, no VBS state appears to be stable on J_1 - J_2 spin-1 square lattice [31]. In fact the only isotropic lattice (that the authors are aware of) appearing to support a VBS state is the honeycomb J_1 - J_2 model, where DMRG calculations find a stable plaquette VBS order [33].

The discontinuous nature of the DVBS quantum melting transition we found precludes the possibility of a deconfined quantum criticality mentioned earlier in the context of spin-1/2 models, in agreement with the finding in Ref. 46 for a more complicated spin-1 model. It is conceivable that the deep reason for the difference in the stability of the VBS phases between spin-1/2 and spin-1 models lies in the Lieb-Schultz-Mattis-Oshikawa-Hastings theorem [47–49], which prohibits existence of gapped non-topological phases in spin-1/2 systems unless the unit cell is doubled due to the dimer formation. There is no such restriction for integer spin systems however, with a featureless correlated paramagnet state possible, which has been suggested in several numerical studies on spin-1 models [15–17, 32]. As the present work indicates, spin-1 models offer a rich palette of quantum phases that deserve future investigation.

We thank Miles Stoudenmire for stimulating discussions and give credit to Shuyi Li for the guidance in the LFWT analysis. Y.X. and A.H.N. acknowledge the support of the National Science Foundation Division of Materials Research under the Award DMR-1917511. T.F. was supported by the Welch Foundation grant no. C-1818. J.H. was supported by the European Research Council (ERC) under the European Union’s Horizon 2020 research and innovation programme (grant agreement No 101001604). The majority of the calculations were performed on the clusters supported by the Big-Data Private-Cloud Research Cyberinfrastructure MRI-award funded by NSF under grant CNS-1338099 and by Rice University’s Center for Research Computing (CRC).

* yx51@rice.edu

† j.hasik@uva.nl

‡ nevidomskyy@rice.edu

- [1] C. K. Majumdar and D. K. Ghosh, On Next-Nearest-Neighbor Interaction in Linear Chain. I, *J. Math. Phys.* **10**, 1388 (1969).
- [2] B. Kumar, Quantum spin models with exact dimer ground states, *Phys. Rev. B* **66**, 024406 (2002).
- [3] S.-S. Gong, W. Zhu, D. Sheng, O. I. Motrunich, and M. P. Fisher, Plaquette Ordered Phase and Quantum Phase Diagram in the spin- $\frac{1}{2}$ $j_1 - j_2$ square Heisenberg model, *Phys. Rev. Lett.* **113**, 027201 (2014).
- [4] L. Wang and A. W. Sandvik, Critical level crossings and gapless spin liquid in the square-lattice spin-1/2 $J_1 - J_2$ heisenberg antiferromagnet, *Phys. Rev. Lett.* **121**, 107202 (2018).
- [5] F. Ferrari and F. Becca, Gapless spin liquid and valence-bond solid in the J_1 - J_2 heisenberg model on the square lattice: Insights from singlet and triplet excitations, *Phys. Rev. B* **102**, 014417 (2020).
- [6] Y. Nomura and M. Imada, Dirac-type nodal spin liquid revealed by refined quantum many-body solver using neural-network wave function, correlation ratio, and level spectroscopy, *Phys. Rev. X* **11**, 031034 (2021).
- [7] W.-Y. Liu, S.-S. Gong, Y.-B. Li, D. Poilblanc, W.-Q. Chen, and Z.-C. Gu, Gapless quantum spin liquid and global phase diagram of the spin-1/2 j_1 - j_2 square antiferromagnetic heisenberg model, *Science Bulletin* **67**, 1034 (2022).
- [8] S.-S. Gong, D. N. Sheng, O. I. Motrunich, and M. P. A. Fisher, Phase diagram of the spin- $\frac{1}{2}$ $j_1 - j_2$ Heisenberg model on a honeycomb lattice, *Phys. Rev. B* **88**, 165138 (2013), publisher: American Physical Society.
- [9] F. Ferrari, S. Bieri, and F. Becca, Competition between spin liquids and valence-bond order in the frustrated spin- $\frac{1}{2}$ Heisenberg model on the honeycomb lattice, *Phys. Rev. B* **96**, 104401 (2017), publisher: American Physical Society.
- [10] P. W. Anderson, Resonating valence bonds: A new kind of insulator?, *Mater. Res. Bull.* **8**, 153 (1973).
- [11] L. Balents, Spin liquids in frustrated magnets, *Nature* **464**, 199 (2010).
- [12] A. V. Chubukov, Chiral, nematic, and dimer states in quantum spin chains, *Phys. Rev. B* **44**, 4693 (1991).
- [13] K. Buchta, G. Fáth, O. Legeza, and J. Sólyom, Probable absence of a quadrupolar spin-nematic phase in the bilinear-biquadratic spin-1 chain, *Phys. Rev. B* **72**, 054433 (2005).
- [14] D. Porras, F. Verstraete, and J. I. Cirac, Renormalization algorithm for the calculation of spectra of interacting quantum systems, *Phys. Rev. B* **73**, 014410 (2006).
- [15] I. Niesen and P. Corboz, A tensor network study of the complete ground state phase diagram of the spin-1 bilinear-biquadratic Heisenberg model on the square lattice, *SciPost Phys.* **3**, 030 (2017).
- [16] I. Niesen and P. Corboz, Ground-state study of the spin-1 bilinear-biquadratic heisenberg model on the triangular lattice using tensor networks, *Phys. Rev. B* **97**, 245146 (2018).
- [17] H. J. Changlani and A. M. Läuchli, Trimerized ground state of the spin-1 heisenberg antiferromagnet on the kagome lattice, *Phys. Rev. B* **91**, 100407 (2015).
- [18] T. Liu, W. Li, A. Weichselbaum, J. von Delft, and G. Su, Simplex valence-bond crystal in the spin-1 kagome heisenberg antiferromagnet, *Phys. Rev. B* **91**, 060403 (2015).
- [19] I. Niesen and P. Corboz, Emergent Haldane phase in the $S = 1$ bilinear-biquadratic Heisenberg model on the square lattice, *Physical Review B* **95**, 10.1103/PhysRevB.95.180404 (2017).
- [20] W.-J. Hu, S.-S. Gong, H.-H. Lai, H. Hu, Q. Si, and A. H. Nevidomskyy, Nematic spin liquid phase in a frustrated spin-1 system on the square lattice, *Phys. Rev. B* **100**, 165142 (2019).
- [21] S. Nakatsuji, Y. Nambu, H. Tonomura, O. Sakai, S. Jonas, C. Broholm, H. Tsunetsugu, Y. Qiu, and Y. Maeno, Spin disorder on a triangular lattice, *Science* **309**, 1697 (2005), <https://www.science.org/doi/pdf/10.1126/science.1114727>.
- [22] S. Bhattacharjee, V. B. Shenoy, and T. Senthil, Possible ferro-spin nematic order in NiGa_2S_4 , *Phys. Rev. B* **74**,

- 092406 (2006).
- [23] H. Tsunetsugu and M. Arikawa, Spin nematic phase in $s=1$ triangular antiferromagnets, *Journal of the Physical Society of Japan* **75**, 083701 (2006), <https://doi.org/10.1143/JPSJ.75.083701>.
- [24] S. Bieri, M. Serbyn, T. Senthil, and P. A. Lee, Paired chiral spin liquid with a fermi surface in $s = 1$ model on the triangular lattice, *Phys. Rev. B* **86**, 224409 (2012).
- [25] B. Fåk, S. Bieri, E. Canévet, L. Messio, C. Payen, M. Viaud, C. Guillot-Deudon, C. Darie, J. Ollivier, and P. Mendels, Evidence for a spinon fermi surface in the triangular $s = 1$ quantum spin liquid $\text{Ba}_3\text{NiSb}_2\text{O}_9$, *Phys. Rev. B* **95**, 060402 (2017).
- [26] T. A. Tóth, A. M. Läuchli, F. Mila, and K. Penc, Three-sublattice ordering of the $\text{su}(3)$ heisenberg model of three-flavor fermions on the square and cubic lattices, *Phys. Rev. Lett.* **105**, 265301 (2010).
- [27] B. Bauer, P. Corboz, A. M. Läuchli, L. Messio, K. Penc, M. Troyer, and F. Mila, Three-sublattice order in the $\text{su}(3)$ heisenberg model on the square and triangular lattice, *Phys. Rev. B* **85**, 125116 (2012).
- [28] A. V. Gorshkov, M. Hermele, V. Gurarie, C. Xu, P. S. Julienne, J. Ye, P. Zoller, E. Demler, M. D. Lukin, and A. M. Rey, Two-orbital s u(n) magnetism with ultracold alkaline-earth atoms, *Nature Physics* **6**, 289 (2010).
- [29] D. S. Rokhsar and S. A. Kivelson, Superconductivity and the Quantum Hard-Core Dimer Gas, *Physical Review Letters* **61**, 2376 (1988).
- [30] R. Moessner and S. L. Sondhi, Resonating Valence Bond Phase in the Triangular Lattice Quantum Dimer Model, *Physical Review Letters* **86**, 1881 (2001).
- [31] R. Haghshenas, W.-W. Lan, S.-S. Gong, and D. N. Sheng, Quantum phase diagram of spin-1 $J_1 - J_2$ heisenberg model on the square lattice: An infinite projected entangled-pair state and density matrix renormalization group study, *Phys. Rev. B* **97**, 184436 (2018).
- [32] H. H. Zhao, C. Xu, Q. N. Chen, Z. C. Wei, M. P. Qin, G. M. Zhang, and T. Xiang, Plaquette order and deconfined quantum critical point in the spin-1 bilinear-biquadratic heisenberg model on the honeycomb lattice, *Phys. Rev. B* **85**, 134416 (2012).
- [33] S.-S. Gong, W. Zhu, and D. N. Sheng, Quantum phase diagram of the spin-1 $J_1 - J_2$ heisenberg model on the honeycomb lattice, *Phys. Rev. B* **92**, 195110 (2015).
- [34] A. Läuchli, G. Schmid, and S. Trebst, Spin nematics correlations in bilinear-biquadratic $s = 1$ spin chains, *Phys. Rev. B* **74**, 144426 (2006).
- [35] J. H. Pixley, A. Shashi, and A. H. Nevidomskyy, Frustration and multicriticality in the antiferromagnetic spin-1 chain, *Physical Review B* **90**, 10.1103/PhysRevB.90.214426 (2014).
- [36] T. Senthil, A. Vishwanath, L. Balents, S. Sachdev, and M. P. A. Fisher, Deconfined quantum critical points, *Science* **303**, 1490 (2004), <https://www.science.org/doi/pdf/10.1126/science.1091806>.
- [37] T. Senthil, L. Balents, S. Sachdev, A. Vishwanath, and M. P. A. Fisher, Quantum criticality beyond the Landau-Ginzburg-Wilson paradigm, *Phys. Rev. B* **70**, 144407 (2004).
- [38] In this work, we shall not consider AKLT-like states for spin-1, which are confusingly sometimes also called VBS states. For the remainder of this work, we will use the term VBS to refer to the translational symmetry broken, dimerized states, sometimes also called spin-Peierls states.
- [39] K. Penc and A. M. Läuchli, Introduction to frustrated magnetism: Materials, experiments, theory (Springer Berlin Heidelberg, Berlin, Heidelberg, 2011) Chap. Spin Nematic Phases in Quantum Spin Systems, pp. 331–362.
- [40] J. Jordan, R. Orús, G. Vidal, F. Verstraete, and J. I. Cirac, Classical simulation of infinite-size quantum lattice systems in two spatial dimensions, *Phys. Rev. Lett.* **101**, 250602 (2008).
- [41] H.-J. Liao, J.-G. Liu, L. Wang, and T. Xiang, Differentiable programming tensor networks, *Phys. Rev. X* **9**, 031041 (2019).
- [42] P. Corboz, T. M. Rice, and M. Troyer, Competing states in the t - j model: Uniform d -wave state versus stripe state, *Phys. Rev. Lett.* **113**, 046402 (2014).
- [43] S. R. White, Density matrix formulation for quantum renormalization groups, *Phys. Rev. Lett.* **69**, 2863 (1992).
- [44] E. Stoudenmire and S. R. White, Studying two-dimensional systems with the density matrix renormalization group, *Annual Review of Condensed Matter Physics* **3**, 111 (2012), <https://doi.org/10.1146/annurev-conmatphys-020911-125018>.
- [45] M. Fishman, S. R. White, and E. M. Stoudenmire, The ITensor software library for tensor network calculations (2020), arXiv:2007.14822.
- [46] J. Wildeboer, N. Desai, J. D’Emidio, and R. K. Kaul, First-order néel to columnar valence bond solid transition in a model square-lattice $s = 1$ antiferromagnet, *Phys. Rev. B* **101**, 045111 (2020).
- [47] E. H. Lieb, T. Schultz, and D. Mattis, Two soluble models of an antiferromagnetic chain, *Ann. Phys.* **16**, 407 (1961).
- [48] M. Oshikawa, Commensurability, Excitation Gap, and Topology in Quantum Many-Particle Systems on a Periodic Lattice, *Phys. Rev. Lett.* **84**, 1535 (2000).
- [49] M. B. Hastings, Lieb-Schultz-Mattis in higher dimensions, *Phys. Rev. B* **69**, 104431 (2004).
- [50] T. Nishino and K. Okunishi, A density matrix algorithm for 3d classical models, *Journal of the Physical Society of Japan* **67**, 3066 (1998), <https://doi.org/10.1143/JPSJ.67.3066>.
- [51] J. Hasik and G. B. Mbeng, peps-torch: A differentiable tensor network library for two-dimensional lattice models, <https://github.com/jurajHasik/peps-torch>.
- [52] W. H. Press, S. A. Teukolsky, W. T. Vetterling, and B. P. Flannery, *Numerical Recipes, The Art of Scientific Computing, 3rd Edition* (Cambridge University Press, Cambridge, 2007).

Supplementary Materials for “ Quantum Melting of Spin-1 Dimer Solid Induced by Inter-chain Couplings ”

INFINITE PROJECTED ENTANGLED-PAIR STATES (IPEPS)

The ground-state wave function is parametrized by a set of rank-5 on-site tensors $\{a_{uldr}^s\}$ associated with physical sites in the unit cell (depending on the spatial pattern) which then tiles the entire square lattice. The physical index s runs over states of $S = 1$ degrees of freedom while u, l, d , and r are auxiliary indices of *bond dimension* D associated with up, left, down and right bonds of each site on the square lattice. The physical wavefunction on (infinite) square lattice is then formally obtained by contracting on-site tensors along pairs of auxiliary indices common to the bonds of the lattice

$$|\psi(\{a\})\rangle = \sum_{\{s\}} \text{Tr}[\dots a^{s-1} a^{s_0} a^{s_1} \dots] |\dots s_{-1} s_0 s_1 \dots\rangle \quad (\text{S1})$$

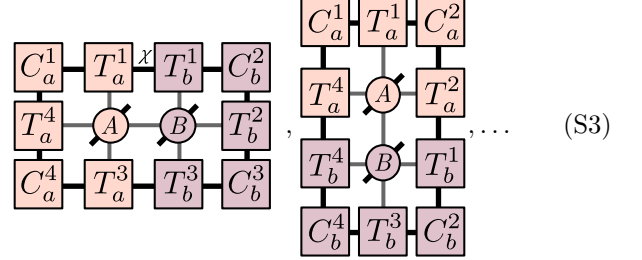
The quality of the approximation is controlled by D , starting from trivial $D = 1$ iPEPS describing only mean-field wave functions to highly-entangled states as D grows. Tractable manipulation of iPEPS is realized by considering only reduced density matrices of finite subsystems, which are sufficient to compute physical quantities of interests such as energy, local order parameters or correlation functions. We construct such reduced density matrices from iPEPS environments which provide finite-dimensional embedding of subsystems. The environments are obtained by the corner transfer matrix renormalization group (CTMRG) algorithm [42, 50], with their precision controlled by *environment* bond dimension χ . For given iPEPS, one recovers its exact reduced density matrices in the limit of $\chi \rightarrow \infty$. To find optimal values for elements of on-site tensors, we perform their gradient-based optimization using automatic differentiation [41]. These simulations were realized using *peps-torch* library [51].

The variational energy per site e of iPEPS state given in Eq. 7 is obtained by evaluating four non-equivalent contributions

$$e = \sum_{i=0,1} \langle J_{\parallel} \mathbf{S}_{i,0} \cdot \mathbf{S}_{i+1,0} + K_{\parallel} (\mathbf{S}_{i,0} \cdot \mathbf{S}_{i+1,0})^2 \rangle + \sum_{j=0,1} \langle J_{\perp} \mathbf{S}_{0,j} \cdot \mathbf{S}_{0,j+1} + K_{\perp} (\mathbf{S}_{0,j} \cdot \mathbf{S}_{0,j+1})^2 \rangle. \quad (\text{S2})$$

To evaluate the above terms, we construct four distinct reduced density matrices (RDMs) of nearest-neighbor sites using environment tensors $\{C, T\}$ obtained from CTMRG. Assuming tensor a is assigned to site $[i, j] = [0, 0]$, the first two RDMs are $\rho_{2 \times 1}([0, 0], [1, 0])$,

$$\rho_{1 \times 2}([0, 1], [0, 2])$$



and the remaining two, $\rho_{2 \times 1}([1, 0], [2, 0])$ and $\rho_{1 \times 2}([0, 0], [0, 1])$, which we do not show can be constructed analogously. Tensors A and B are double-layer tensors obtained by contracting the physical index, i.e., $A_{(uu')(ll')(dd')(rr')} = \sum_s a_{uldr}^s a_{u'l'd'r'}^{*s}$, while sites with open physical indices, $A_{(uu')(ll')(dd')(rr')}^{ss'} = a_{uldr}^s a_{u'l'd'r'}^{*s'}$, have diagonal black lines.

The optimization is done by repeating four steps: (i) perform CTMRG for state $|\psi(a, b)\rangle$ and obtain environment tensors $\{C, T\}$, (ii) evaluate variational energy e , (iii) compute gradients $g_a = \partial e / \partial a$, $g_b = \partial e / \partial b$, (iv) update tensors a and b using L-BFGS method with a backtracking line search. The optimization terminates once the relative difference in variational energies between consecutive steps becomes lower than 10^{-8} . For details regarding L-BFGS gradient descent, which is a quasi-Newton method constructing an approximate Hessian from past gradients, and line search see Ref. [52].

In the main text, we have used exclusively bipartite tiling of the square lattice with 2×1 unit cell. In the dimerized phase this choice leads to *staggered* dimer state (svBS). The second option is to use stripe tiling, where horizontal dimers are aligned in columns (cvBS). We have verified, that these two choices are very close in energies in the dimer phase. For example, at $(\theta, r) = (-0.5625\pi, 0.02)$, with $D_x = 9$, $D_y = 4$ and $\chi = 16$, $e_{\text{svBS}} = -2.558822$, $E_{\text{cvBS}} = -2.558595$.

Although the dimerized phase of coupled spin-1 chains is gapped, its accurate description in terms of iPEPS requires a relatively large bond dimension. We study the limiting case of iPEPS ansatz with $D_y = 1$, which in effect parametrizes the ground state of decoupled chains ($r = 1$) as a product state of MPS with bond dimension D_x for each individual spin-1 chain. In Fig. S1 we show the breaking of expected $SU(2)$ symmetry through non-vanishing expectation values of m , II_Q , and III_Q as function of $1/D_x$. This computation reveals that $D_x \geq 9$ is necessary to obtain a good approximation of the ground state even in this simple limit, since iPEPS with smaller D_x display substantial breaking of $SU(2)$ either by devel-

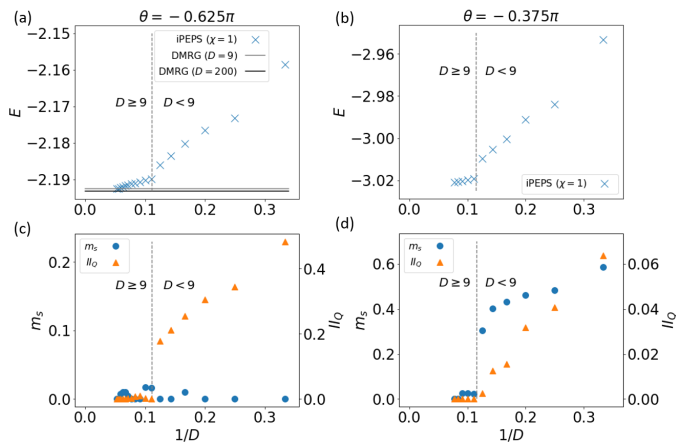


FIG. S1. Spurious SU(2)-symmetry breaking induced by finite- D effects in dimerized phase of decoupled chains, $r = 0$, for $\theta = -5/8\pi$ (left) and $\theta = -3/8\pi$ (right). Keeping $D_y = 1$, for $D_x \geq 9$ all order parameters m_s and II_Q become small.

oping large magnetization or higher moments II_Q , III_Q .

DENSITY MATRIX RENORMALIZATION GROUP (DMRG)

Subtleties in defining the Néel order parameters on finite systems

In the main text, the order parameter for Néel phase is defined as the staggered magnetization, which is not an SU(2)-invariant observable. This will cause trouble when studying the SU(2) symmetry broken states in finite size systems because the SU(2) symmetry can only be broken in the thermodynamic limits. Specifically speaking, the DMRG algorithm that deals with the finite size cylinders does not have a preference on the choice of symmetry breaking "direction". As a result, in practice one may end up with states which are some linear superposition of different symmetry broken states, or even SU(2)-symmetric states. If the state is SU(2)-symmetric, the U(1)-symmetric staggered magnetization will apparently be vanishing. In our case, this situation corresponds to the simulations for the cut B ($\theta = -0.4375\pi$) which was initialized by the DVBS states (the simulations initialized by the Néel AFM states do not suffer from the problem since the initial states have already broken the SU(2) spin-rotation symmetry).

To resolve this issue with DMRG on finite cylinders, we apply the pinning fields of Néel type at boundaries [44] to explicitly break the global spin-rotation symmetry without disrupting too much the bulk physics. The pinning field strength is $|h_{\text{Néel}}^{\text{pin}}| = 0.5$.

Finite size scaling

In the main context, we show the finite size scaling plot for cut B initialized by the Néel AFM state, in Fig. 3. Here, we also attach the result for cut A with the FQ initial state. Given that the exponential decaying edge effects, we use an exponential fitting form versus the cylinder length N_x introduced by [13] for finite size extrapolation in our analysis.

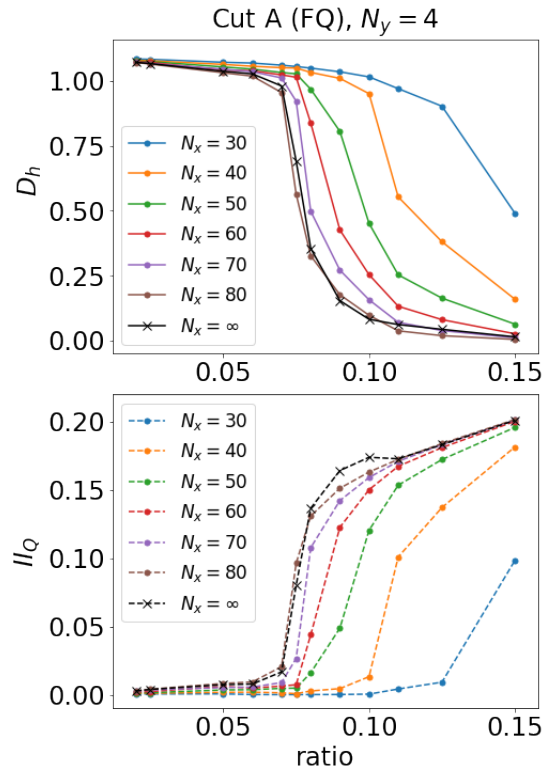


FIG. S2. Finite size scaling of order parameters D_h and II_Q versus N_x for cut A initialized by $|FQ\rangle$.

In this work, DMRG simulations are performed systematically mainly for $N_y = 4$, because we are more interested in the coupled chains behavior, and the computational cost of finite size scaling versus N_y is very expensive. Here, we present how the dimerized order melts as ratio increases for fixed $N_x = 30$ and different N_y 's (with $M = 2000$ states kept, truncation errors $N_y = 4, 5, 6$ simulations are $\varepsilon_{N_y=4} < 2 \times 10^{-5}$, $\varepsilon_{N_y=5} < 5 \times 10^{-5}$, $\varepsilon_{N_y=6} < 3 \times 10^{-5}$), as shown by Fig. S3. As N_y increases, the DVBS melting transition may happen at different ratios ($r = 0.06$ 0.1) for different N_y 's, but this do not qualitatively change our conclusion that the DVBS order melts very quickly.

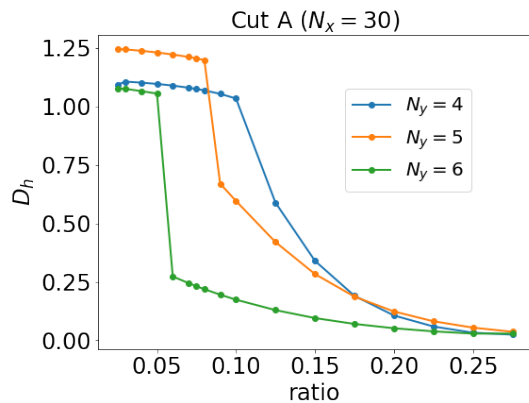


FIG. S3. Melting of the dimerized order for different cylinder circumferences for cut A and fixed $N_x = 30$.

ENERGY LEVEL CROSSINGS

In iPEPS and DMRG simulations, the simulations for each θ were initialized by two different states which represent different orders of the 1D- and 2D-limit phases. Apart from the hysteretic melting process of the DVBS order, we also observe the energy level crossings. By making use of this, we determine the phase boundary of the DVBS phase by the crossing points. Here, we show the energy level crossings (the energy difference) for both cuts A and B where both iPEPS and DMRG results are present, as shown by Fig. S4. Also, note that for DMRG results, we first extrapolated the energies in the $N_x \rightarrow \infty$ using the linear fitting function. The blue and orange dashed lines represent the "virtual" energies that are obtained by evaluating the Hamiltonian at some ratio r yet using the states at r_1 and r_2 .

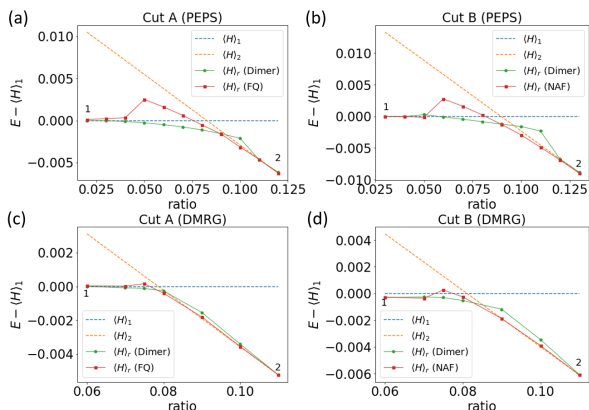


FIG. S4. (a)-(d) Energy level crossings using different initial states for cuts A and B. $\langle H \rangle_{1,2}$ are computed using the state at r_1 initialized by $|DVBS\rangle$ at and the state at r_2 initialized by $|FQ\rangle$ for cut A or $|NAF\rangle$ for cut B.

CORRELATION FUNCTIONS AND CORRELATION LENGTHS

We computed different types of correlation functions including the spin-spin, dimer-dimer and quadrupole-quadrupole correlation functions ($C_S(r)$, $C_D(r)$ and $C_Q(r)$) for cuts A and B.

The spin-spin correlation is simply defined as

$$C_S(r) = \langle \mathbf{S}(r) \cdot \mathbf{S}(0) \rangle, \quad (S4)$$

The dimer-dimer correlation function is defined as the product of two dimers, $D(0)$ and $D(r)$, given by (note that they are different from the dimer order parameter D_h). The two dimers should not overlap with each other, which means that the position of the nearest dimer should be shifted by 2 with respect to the reference dimer.

$$C_D(r) = \langle D((r+1)\mathbf{x})D(0) \rangle, \quad (S5)$$

where the dimer is defined as $D(r) = \mathbf{S}(r) \cdot \mathbf{S}(r+\mathbf{x})$.

The quadrupole-quadrupole correlation function is given by

$$C_Q(r) = \langle \mathbf{Q}(r) \cdot \mathbf{Q}(0) \rangle, \quad (S6)$$

where the quadrupolar operator \mathbf{Q} , as a generalization of the spin vector for magnetic order, describes the quadrupolar order of spin-1 states, and is given by [39]

$$\mathbf{Q} = \begin{pmatrix} Q^{x^2-y^2} \\ Q^{3z^2-r^2} \\ Q^{xy} \\ Q^{yz} \\ Q^{zx} \end{pmatrix} = \begin{pmatrix} (S^x)^2 - (S^y)^2 \\ \frac{1}{\sqrt{3}}[3(S^z)^2 - S(S+1)] \\ S^x S^y + S^y S^x \\ S^y S^z + S^z S^y \\ S^x S^z + S^z S^x \end{pmatrix} \quad (S7)$$

To extract the correlation lengths, we compute the connected version of correlation functions,

$$C_{\mathcal{O}}^C(r) = \langle \mathcal{O}(0) \cdot \mathcal{O}(r) \rangle - \langle \mathcal{O}(0) \rangle \cdot \langle \mathcal{O}(r) \rangle \quad (S8)$$

(for the operator $\mathcal{O} = \mathbf{S}, \mathbf{Q}$, or D). We present the results of the connected correlation functions at two ratios for both cut A and cut B, as shown by Fig. S5(a,c) and Fig. S6(a,c). Then, the Ornstein-Zernike formula is used to extract the correlation lengths for both cuts, as shown in Fig. S5(b,d) and Fig. S6(b,d). In the vicinity of the phase boundary, we do not observe any singular behaviors for all the connected correlation function, excluding the possibility of continuous phase transition. The spin-spin and quadrupolar-quadrupolar correlation lengths are correspondingly finite in the DVBS phase, as shown in Fig. S6(c,d). The same is true of the dimer correlation length ξ_D in Fig. S5(c,d), which is extracted from the long-distance tail of the dimer-dimer correlation function (after the short-range transient component decays).

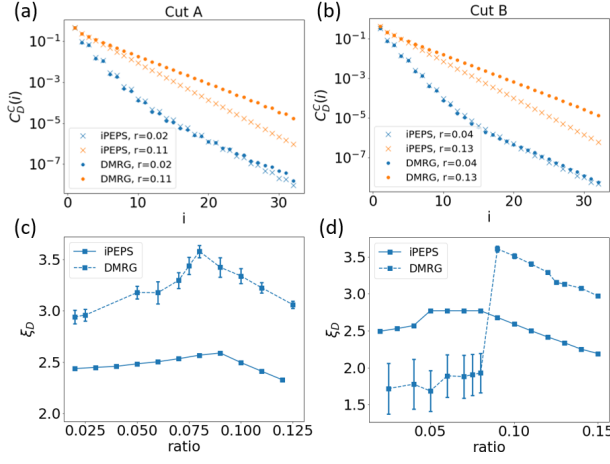


FIG. S5. (a,b) Connected dimer-dimer correlation functions at two ratios deeply in the two phases for cuts A and B. (c,d) Dimer-dimer correlation lengths for the two cuts.

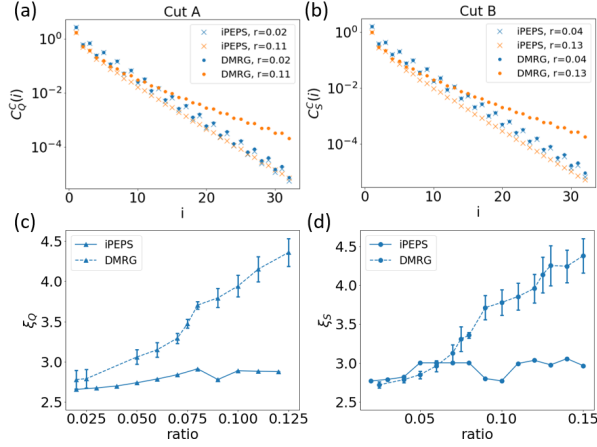


FIG. S6. (a,b) Connected quadrupole-quadrupole or spin-spin correlation functions at two ratios for the two cuts. (c,d) Quadrupole-Quadrupole and spin-spin correlation lengths for the two cuts.

MEAN-FIELD RESULT

Consider the following Hamiltonian for general spin- S .

$$H = \frac{1}{S^2} \sum_{i,j} \left[J_{\parallel} \mathbf{S}_{i,j} \cdot \mathbf{S}_{i+1,j} + K_{\parallel} (\mathbf{S}_{i,j} \cdot \mathbf{S}_{i+1,j})^2 + J_{\perp} \mathbf{S}_{i,j} \cdot \mathbf{S}_{i,j+1} + K_{\perp} (\mathbf{S}_{i,j} \cdot \mathbf{S}_{i,j+1})^2 \right] \quad (\text{S9})$$

where $J_{\parallel} = \cos \theta$, $K_{\parallel} = \sin \theta$, $J_{\perp} = r \cos \theta$, $K_{\perp} =$

$r \sin \theta$. The biquadratic term can be expanded as follow.

$$\begin{aligned} (\mathbf{S}_1 \cdot \mathbf{S}_2)^2 &= \frac{1}{4} \underbrace{S_{1+} S_{1+} S_{2-} S_{2-}} + \frac{1}{4} \underbrace{S_{1+} S_{1-} S_{2-} S_{2+}} \\ &+ \frac{1}{2} S_{1+} S_{1z} S_{2-} S_{2z} + \frac{1}{4} \underbrace{S_{1-} S_{1+} S_{2+} S_{2-}} \\ &+ \frac{1}{4} \underbrace{S_{1-} S_{1-} S_{2+} S_{2+}} + \frac{1}{2} S_{1-} S_{1z} S_{2+} S_{2z} \\ &+ \frac{1}{2} S_{1z} S_{1+} S_{2z} S_{2-} + \frac{1}{2} S_{1z} S_{1-} S_{2z} S_{2+} \\ &+ \underbrace{S_{1z} S_{1z} S_{2z} S_{2z}} \end{aligned} \quad (\text{S10})$$

For Néel and dimerized state, only the underlined terms can have non-trivial contributions (S11,S15,S19) because they do not change the onsite S_z quantum numbers. For the $S = 1$ SN state (FQ), if one chooses $|x\rangle$ or $|y\rangle$, the wavy underlined terms will also contribute (S14).

Néel AFM

$$\begin{aligned} \langle S\bar{S} | \mathbf{S}_1 \cdot \mathbf{S}_2 | S\bar{S} \rangle &= -S^2 \\ \langle S\bar{S} | (\mathbf{S}_1 \cdot \mathbf{S}_2)^2 | S\bar{S} \rangle &= \frac{1}{4} \sqrt{2S} \sqrt{2S} + S^2 (-S)^2 \\ &= S^4 + S^2 \end{aligned} \quad (\text{S11})$$

Spin-nematic (FQ) ($S \geq 1$)

$$|\psi_{FQ}\rangle = |\phi^S\rangle = \frac{1}{\sqrt{2}} (|S\rangle + |\bar{S}\rangle) \quad (\text{S12})$$

$$\langle \phi_1^S \phi_2^S | \mathbf{S}_1 \cdot \mathbf{S}_2 | \phi_1^S \phi_2^S \rangle = 0 \quad (\text{S13})$$

$S = 1$:

$$\begin{aligned} \langle \phi_1^S \phi_2^S | (\mathbf{S}_1 \cdot \mathbf{S}_2)^2 | \phi_1^S \phi_2^S \rangle &= 2 \times \frac{1}{4} \left(\frac{2S}{2}\right)^2 + 2 \times \frac{1}{4} \left(\frac{2S}{2}\right)^2 + S^4 \\ &= S^4 + S^2 = 2 \end{aligned} \quad (\text{S14})$$

$S > 1$:

$$\begin{aligned} \langle \phi_1^S \phi_2^S | (\mathbf{S}_1 \cdot \mathbf{S}_2)^2 | \phi_1^S \phi_2^S \rangle &= 2 \times \frac{1}{4} \left(\frac{2S}{2}\right)^2 + S^4 \\ &= S^4 + \frac{1}{2} S^2 \end{aligned} \quad (\text{S15})$$

Dimerized VBS

Note that there are two degenerate ground states for the dimerized (DVBS) order on the spin chain due to the translational symmetry breaking. The energy per site for the dimerized state should be averaged.

For the two spins from one dimer,

$$|S_{tot} = 0\rangle = \frac{1}{\sqrt{2S+1}} \sum_{m=-S}^S (-1)^{S-m} |m\rangle_1 |S-m\rangle_2 \quad (\text{S16})$$

Since $2\mathbf{S}_1 \cdot \mathbf{S}_2 = (\mathbf{S}_1 + \mathbf{S}_2)^2 - \mathbf{S}_1^2 - \mathbf{S}_2^2$, we have

$$\begin{aligned} \langle S_{tot} = 0 | \mathbf{S}_1 \cdot \mathbf{S}_2 | S_{tot} = 0 \rangle &= -S(S+1) \\ \langle S_{tot} = 0 | (\mathbf{S}_1 \cdot \mathbf{S}_2)^2 | S_{tot} = 0 \rangle &= S^2(S+1)^2 \end{aligned} \quad (\text{S17})$$

For the two spins from two different dimers,

$$\langle S_{tot}^{13} = 0 | \langle S_{tot}^{24} = 0 | \mathbf{S}_1 \cdot \mathbf{S}_2 | S_{tot}^{13} = 0 \rangle | S_{tot}^{24} = 0 \rangle = 0 \quad (\text{S18})$$

$$\begin{aligned} &\langle S_{tot}^{13} = 0 | \langle S_{tot}^{24} = 0 | (\mathbf{S}_1 \cdot \mathbf{S}_2)^2 | S_{tot}^{13} = 0 \rangle | S_{tot}^{24} = 0 \rangle \\ &= \frac{2}{4} \times \left\{ \frac{1}{2S+1} \sum_{m=-S}^{S-1} [S(S+1) - m(m+1)] \right. \\ &\quad \times \left. \frac{1}{2S+1} \sum_{m=-S+1}^S [S(S+1) - m(m-1)] \right\} \\ &\quad + \left[\frac{1}{2S+1} \sum_{m=-S}^S m^2 \right]^2 = \frac{1}{3} S^2(S+1)^2 \end{aligned} \quad (\text{S19})$$

With the information above, we then have the expressions for the mean-field ansatz. The mean-field phase diagram is shown by Fig. S7.

$$E_{\text{NAF}}^{\text{mf}} = -(1+r) \cos \theta + (S^2+1)(1+r) \sin \theta \quad (\text{S20})$$

$$E_{\text{DVBS}}^{\text{mf}} = -\frac{S+1}{2S} \cos \theta + \frac{(S+1)^2}{3} (2+r) \sin \theta \quad (\text{S21})$$

$$E_{\text{FQ}}^{\text{mf}} = (S^2 + \frac{1}{2} + \frac{1}{2}\Theta(\frac{5}{4} - S))(1+r) \sin \theta \quad (\text{S22})$$

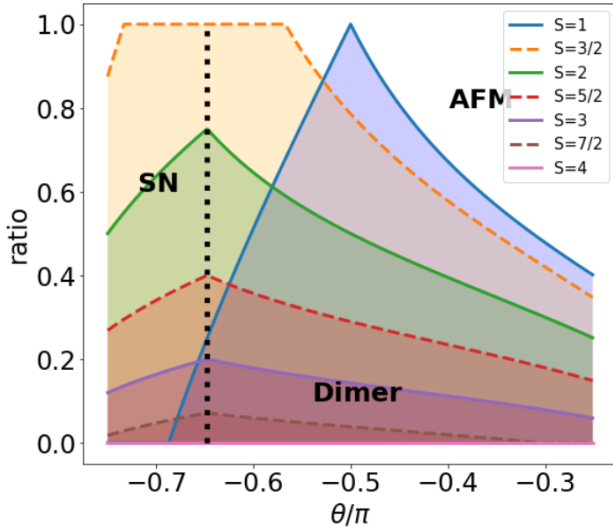


FIG. S7. Mean-field phase diagram for spin-S BBH coupled chains with $\theta \in [-3\pi/4, -\pi/4]$. The shaded region indicates the dimerized phase. The solid lines indicate the boundaries for integer spins, and the dashed lines represent the boundaries for half integer spins.

LINEAR FLAVOR WAVE THEORY

Consider $S = 1$ case. The Hamiltonian is given by

$$\begin{aligned} H &= \sum_{i,j} \left[J_{\parallel} \mathbf{S}_{i,j} \cdot \mathbf{S}_{i+1,j} + K_{\parallel} (\mathbf{S}_{i,j} \cdot \mathbf{S}_{i+1,j})^2 \right] \\ &\quad + \sum_{i,j} \left[J_{\perp} \mathbf{S}_{i,j} \cdot \mathbf{S}_{i,j+1} + K_{\perp} (\mathbf{S}_{i,j} \cdot \mathbf{S}_{i,j+1})^2 \right] \end{aligned} \quad (\text{S23})$$

Flavor wave boson representation (dipolar basis)

In the dipolar (S_z) basis, the matrix form for operators \mathbf{S} and \mathbf{Q} are

$$\begin{aligned} S^x &= \frac{1}{\sqrt{2}} \begin{bmatrix} 0 & 1 & 0 \\ 1 & 0 & 1 \\ 0 & 1 & 0 \end{bmatrix}, & S^y &= \frac{1}{\sqrt{2}} \begin{bmatrix} 0 & -i & 0 \\ i & 0 & -i \\ 0 & i & 0 \end{bmatrix}, \\ S^z &= \begin{bmatrix} 1 & 0 & 0 \\ 0 & 0 & 0 \\ 0 & 0 & -1 \end{bmatrix}, & Q^{x^2-y^2} &= \begin{bmatrix} 0 & 0 & 1 \\ 0 & 0 & 0 \\ 1 & 0 & 0 \end{bmatrix}, \\ Q^{3z^2-r^2} &= \frac{1}{\sqrt{3}} \begin{bmatrix} 1 & 0 & 0 \\ 0 & -2 & 0 \\ 0 & 0 & 1 \end{bmatrix}, & Q^{xy} &= \begin{bmatrix} 0 & 0 & -i \\ 0 & 0 & 0 \\ i & 0 & 0 \end{bmatrix}, \\ Q^{yz} &= \frac{1}{\sqrt{2}} \begin{bmatrix} 0 & -i & 0 \\ i & 0 & i \\ 0 & -i & 0 \end{bmatrix}, & Q^{zx} &= \frac{1}{\sqrt{2}} \begin{bmatrix} 0 & 1 & 0 \\ 1 & 0 & -1 \\ 0 & -1 & 0 \end{bmatrix} \end{aligned} \quad (\text{S24})$$

Switching to the bosonic language, the operators \mathbf{S} and \mathbf{Q} can be written in terms of the bosonic creation/annihilation operator, i.e.,

$$\begin{aligned} S_i^x &= \frac{1}{\sqrt{2}} (a_i^{1\dagger} a_i^0 + a_i^{0\dagger} a_i^1 + a_i^{0\dagger} a_i^{-1} + a_i^{-1\dagger} a_i^0) \\ S_i^y &= \frac{1}{\sqrt{2}} (-i a_i^{1\dagger} a_i^0 + i a_i^{0\dagger} a_i^1 - i a_i^{0\dagger} a_i^{-1} + i a_i^{-1\dagger} a_i^0) \\ S_i^z &= a_i^{1\dagger} a_i^1 - a_i^{-1\dagger} a_i^{-1} \\ Q_i^{x^2-y^2} &= a_i^{1\dagger} a_i^1 + a_i^{-1\dagger} a_i^{-1} \\ Q_i^{3z^2-r^2} &= \frac{1}{\sqrt{3}} (a_i^{1\dagger} a_i^1 + a_i^{-1\dagger} a_i^{-1} - 2 a_i^{0\dagger} a_i^0) \\ Q_i^{xy} &= -i a_i^{1\dagger} a_i^{-1} + i a_i^{-1\dagger} a_i^1 \\ Q_i^{yz} &= \frac{1}{\sqrt{2}} (-i a_i^{1\dagger} a_i^0 + i a_i^{0\dagger} a_i^1 + i a_i^{0\dagger} a_i^{-1} - i a_i^{-1\dagger} a_i^0) \\ Q_i^{zx} &= \frac{1}{\sqrt{2}} (a_i^{1\dagger} a_i^0 + a_i^{0\dagger} a_i^1 - a_i^{0\dagger} a_i^{-1} - a_i^{-1\dagger} a_i^0) \end{aligned} \quad (\text{S25})$$

Flavor wave boson representation (quadrupolar basis)

In the quadrupolar basis ($|\alpha\rangle, \alpha = x, y, z$), the matrix form for operators \mathbf{S} and \mathbf{Q} are

$$\begin{aligned}
S^x &= \frac{1}{\sqrt{2}} \begin{bmatrix} 0 & 0 & 0 \\ 0 & 0 & -i \\ 0 & i & 0 \end{bmatrix}, & S^y &= \frac{1}{\sqrt{2}} \begin{bmatrix} 0 & 0 & i \\ 0 & 0 & 0 \\ -i & 0 & 0 \end{bmatrix}, \\
S^z &= \begin{bmatrix} 0 & -i & 0 \\ i & 0 & 0 \\ 0 & 0 & 0 \end{bmatrix}, & Q^{x^2-y^2} &= \begin{bmatrix} -1 & 0 & 0 \\ 0 & 1 & 0 \\ 0 & 0 & 0 \end{bmatrix}, \\
Q^{3z^2-r^2} &= \frac{1}{\sqrt{3}} \begin{bmatrix} 1 & 0 & 0 \\ 0 & 1 & 0 \\ 0 & 0 & -2 \end{bmatrix}, & Q^{xy} &= \begin{bmatrix} 0 & -1 & 0 \\ -1 & 0 & 0 \\ 0 & 0 & 0 \end{bmatrix}, \\
Q^{yz} &= \frac{1}{\sqrt{2}} \begin{bmatrix} 0 & 0 & 0 \\ 0 & 0 & -1 \\ 0 & -1 & 0 \end{bmatrix}, & Q^{zx} &= \frac{1}{\sqrt{2}} \begin{bmatrix} 0 & 0 & -1 \\ 0 & 0 & 0 \\ -1 & 0 & 0 \end{bmatrix}
\end{aligned} \tag{S26}$$

Similar to the case in the dipolar basis, in the quadrupolar basis, the operators \mathbf{S} and \mathbf{Q} can be expressed as follows.

$$\begin{aligned}
S_i^x &= -ia_i^{y\dagger} a_i^z + ia_i^{z\dagger} a_i^y \\
S_i^y &= -ia_i^{z\dagger} a_i^x + ia_i^{x\dagger} a_i^z \\
S_i^z &= -ia_i^{x\dagger} a_i^y + ia_i^{y\dagger} a_i^x \\
Q_i^{x^2-y^2} &= -a_i^{x\dagger} a_i^x + a_i^{y\dagger} a_i^y \\
Q_i^{3z^2-r^2} &= \frac{1}{\sqrt{3}} (a_i^{x\dagger} a_i^x + a_i^{y\dagger} a_i^y - 2a_i^{z\dagger} a_i^z) \\
Q_i^{xy} &= -a_i^{x\dagger} a_i^y - a_i^{y\dagger} a_i^x \\
Q_i^{yz} &= -a_i^{y\dagger} a_i^z - a_i^{z\dagger} a_i^y \\
Q_i^{zx} &= -a_i^{z\dagger} a_i^x - a_i^{x\dagger} a_i^z
\end{aligned} \tag{S27}$$

Néel phase

For the Néel AFM state, we choose $|1\rangle$ for A sublattice and $|-1\rangle$ for B sublattice. Then, we can replace a_i^1 and b_i^{-1} by

$$\begin{aligned}
a_i^1 &= a_i^{1\dagger} = \sqrt{M - a_i^{0\dagger} a_i^0 - a_i^{-1\dagger} a_i^{-1}} \\
&\approx \sqrt{M} - \frac{1}{2\sqrt{M}} a_i^{0\dagger} a_i^0 - \frac{1}{2\sqrt{M}} a_i^{-1\dagger} a_i^{-1}
\end{aligned} \tag{S28}$$

$$\begin{aligned}
b_i^{-1} &= b_i^{-1\dagger} = \sqrt{M - b_i^{0\dagger} b_i^0 - b_i^{1\dagger} b_i^1} \\
&\approx \sqrt{M} - \frac{1}{2\sqrt{M}} a_i^{0\dagger} a_i^0 - \frac{1}{2\sqrt{M}} a_i^{-1\dagger} a_i^{-1}
\end{aligned} \tag{S29}$$

here $M = 1$ for $S = 1$. Then, we only keep terms up to the bilinear order for the interaction terms $\mathbf{S}_i \cdot \mathbf{S}_j$ and

$\mathbf{Q}_i \cdot \mathbf{Q}_j = 2(\mathbf{S}_i \cdot \mathbf{S}_j)^2 + \mathbf{S}_i \cdot \mathbf{S}_j - 8/3$. By doing such, we can get

$$\begin{aligned}
H_{(ij)\eta}^{AB} &= (J_\eta - K_\eta)(a_i^{0\dagger} a_i^0 + a_i^{0\dagger} a_i^0 + b_j^{0\dagger} b_j^0 + a_i^0 b_j^0 + a_i^{0\dagger} b_j^{0\dagger}) \\
&\quad + (2J_\eta - K_\eta)(a_i^{-1\dagger} a_i^{-1} + b_j^{1\dagger} b_j^1) \\
&\quad + K_\eta(a_i^{-1} b_j^1 + a_i^{-1\dagger} b_j^{1\dagger}) + (-J_\eta + 2K_\eta)
\end{aligned} \tag{S30}$$

where $\eta = \parallel, \perp$. After that, we perform Fourier transformation $f_i = N^{-1} \sum_{\mathbf{k}} f_{\mathbf{k}} \exp(-i\mathbf{k} \cdot \mathbf{r}_i)$ and then obtain the energy with quantum fluctuation.

$$\begin{aligned}
E &= E_{MF}^0 + \sum_{\mathbf{k}} [a_{\mathbf{k}}^{0\dagger}, b_{-\mathbf{k}}^0] H_1(\mathbf{k}) [a_{\mathbf{k}}^0, b_{-\mathbf{k}}^{0\dagger}] \\
&\quad + [a_{\mathbf{k}}^{-1\dagger}, b_{-\mathbf{k}}^1] H_2(\mathbf{k}) [a_{\mathbf{k}}^{-1}, b_{-\mathbf{k}}^{1\dagger}] - f_{1\mathbf{k}} - f_{2\mathbf{k}}
\end{aligned} \tag{S31}$$

where

$$H_i(\mathbf{k}) = \begin{bmatrix} f_{i\mathbf{k}} & g_{i\mathbf{k}} \\ g_{i\mathbf{k}} & f_{i\mathbf{k}} \end{bmatrix}, i = 1, 2 \tag{S32}$$

with

$$\begin{aligned}
f_{1\mathbf{k}} &= 2(J_{\parallel} - K_{\parallel}) + 2(J_{\perp} - K_{\perp}) \\
g_{1\mathbf{k}} &= 2(J_{\parallel} - K_{\parallel}) \cos k_x + 2(J_{\perp} - K_{\perp}) \cos k_y \\
f_{2\mathbf{k}} &= 2(2J_{\parallel} - K_{\parallel}) + 2(2J_{\perp} - K_{\perp}) \\
g_{2\mathbf{k}} &= 2K_{\parallel} \cos k_x + 2K_{\perp} \cos k_y
\end{aligned} \tag{S33}$$

By doing the Bogoliubov diagonalization, the energy expression becomes

$$\begin{aligned}
E &= E_{MF}^0 + \frac{1}{2} \sum_{\mathbf{k}} [\omega_{1\mathbf{k}} (\alpha_{\mathbf{k}}^\dagger \alpha_{\mathbf{k}} + \beta_{\mathbf{k}}^\dagger \beta_{\mathbf{k}} + 1) - f_{1\mathbf{k}} \\
&\quad + \omega_{2\mathbf{k}} (\gamma_{\mathbf{k}}^\dagger \gamma_{\mathbf{k}} + \eta_{\mathbf{k}}^\dagger \eta_{\mathbf{k}} + 1) - f_{2\mathbf{k}}]
\end{aligned} \tag{S34}$$

where $\omega_{i\mathbf{k}} = \sqrt{f_{i\mathbf{k}}^2 - g_{i\mathbf{k}}^2}$ are the energy eigenvalues.

Thus, the correction to the mean-field energy is

$$\begin{aligned}
\Delta E &= \frac{1}{2} \sum_{\mathbf{k}} (\omega_{1\mathbf{k}} + \omega_{2\mathbf{k}} - f_{1\mathbf{k}} - f_{2\mathbf{k}}) \\
&= \frac{1}{2} \frac{1}{(2\pi)^2} \int_{BZ} d\mathbf{k} (\omega_{1\mathbf{k}} + \omega_{2\mathbf{k}} - f_{1\mathbf{k}} - f_{2\mathbf{k}})
\end{aligned} \tag{S35}$$

FQ phase

For the FQ case, we choose $|z\rangle$ for all the sites. Then, we can replace a_i^z by

$$\begin{aligned}
a_i^z &= a_i^{z\dagger} = \sqrt{M - a_i^{x\dagger} a_i^x - a_i^{y\dagger} a_i^y} \\
&\approx \sqrt{M} - \frac{1}{2\sqrt{M}} a_i^{x\dagger} a_i^x - \frac{1}{2\sqrt{M}} a_i^{y\dagger} a_i^y
\end{aligned} \tag{S36}$$

here $M = 1$ for $S = 1$. Then, again, we only keep terms up to the bilinear order, $O(M)$, for the interaction terms

and perform the Fourier transform. In this way, one can obtain the energy expression in momentum space.

$$E = E_{MF}^0 + \frac{1}{2} \sum_{\mathbf{k}} [f_{\mathbf{k}}(a_{\mathbf{k}}^{x\dagger} a_{\mathbf{k}}^x + a_{-\mathbf{k}}^{x\dagger} a_{-\mathbf{k}}^x + a_{\mathbf{k}}^{y\dagger} a_{\mathbf{k}}^y + a_{-\mathbf{k}}^{y\dagger} a_{-\mathbf{k}}^y) + g_{\mathbf{k}}(a_{\mathbf{k}}^{x\dagger} a_{-\mathbf{k}}^{x\dagger} + a_{\mathbf{k}}^x a_{-\mathbf{k}}^x + a_{\mathbf{k}}^{y\dagger} a_{-\mathbf{k}}^{y\dagger} + a_{\mathbf{k}}^y a_{-\mathbf{k}}^y)] \quad (\text{S37})$$

with

$$\begin{aligned} f_{\mathbf{k}} &= -2(K_{\parallel} + K_{\perp}) + 2(J_{\parallel} \cos k_x + K_{\perp} \cos k_y) \\ g_{\mathbf{k}} &= 2(-J_{\parallel} + K_{\parallel}) \cos k_x + 2(-J_{\perp} + K_{\perp}) \cos k_y \end{aligned} \quad (\text{S38})$$

By doing the Bogoliubov diagonalization, we get

$$E = E_{MF}^0 + \frac{1}{2} \sum_{\mathbf{k}} [\omega_{\mathbf{k}}(\alpha_{\mathbf{k}}^{\dagger} \alpha_{\mathbf{k}} + \alpha_{\mathbf{k}}^{\dagger} \alpha_{\mathbf{k}} + 1) - f_{\mathbf{k}} + \beta_{2\mathbf{k}}(\beta_{\mathbf{k}}^{\dagger} \gamma_{\mathbf{k}} + \beta_{\mathbf{k}}^{\dagger} \beta_{\mathbf{k}} + 1) - f_{\mathbf{k}}] \quad (\text{S39})$$

where $\omega_{\mathbf{k}} = \sqrt{f_{\mathbf{k}}^2 - g_{\mathbf{k}}^2}$ are the energy eigenvalues.

Thus, the correction to the FQ mean-field energy is

$$\Delta E = \sum_{\mathbf{k}} (\omega_{\mathbf{k}} - f_{\mathbf{k}}) = \frac{1}{(2\pi)^2} \int_{BZ} d\mathbf{k} (\omega_{\mathbf{k}} - f_{\mathbf{k}}) \quad (\text{S40})$$